Surface-Modified Titanium Fibers as Durable Carbon-Free Platinum Catalyst Supports for Polymer Electrolyte Fuel Cells

D. Kawachino,[1] M. Yasutake,[1] Z. Noda,[2] J. Matsuda,[2,3] S. M. Lyth,[4,5,6] A. Hayashi,[1,2,3,4,*] and K. Sasaki[1,2,3,4,5,7,*,z]

[1]*Department of Hydrogen Energy Systems, Faculty of Engineering, Kyushu University, Nishi-ku, Fukuoka, 819-0395, Japan*
[2]*International Research Center for Hydrogen Energy, Kyushu University, Nishi-ku, Fukuoka, 819-0395, Japan*
[3]*Next-Generation Fuel Cell Research Center (NEXT-FC), Kyushu University, Nishi-ku, Fukuoka, 819-0395, Japan*
[4]*Platform of Inter/Transdisciplinary Energy Research (Q-PIT), Kyushu University, Nishi-ku, Fukuoka, 819-0395, Japan*
[5]*International Institute for Carbon-Neutral Energy Research (WPI-I^{2}CNER), Kyushu University, Nishi-ku, Fukuoka, 819-0395, Japan*
[6]*Department of Automotive Science, Graduate School of Integrated Frontier Science, Kyushu University, Nishi-ku, Fukuoka, 819-0395, Japan*
[7]*Center of Coevolutionary Research for Sustainable Communities (C^{2}RCS), Kyushu University, Nishi-ku, Fukuoka, 819-0395, Japan*

Carbon-based electrodes in polymer electrolyte fuel cells (PEFCs) are prone to corrosion. Therefore, alternative "carbon-free" materials are required. Here, the use of a catalyst-coated porous metal support is proposed as a gas diffusion electrode. As a proof-of-concept, commercially available porous titanium sheets comprising sintered titanium fibers are chemically etched with NaOH, followed by heat treatment. This results in the formation of oxidized titanium nanostructures (such as nanosheets and nanotubes) at the surface. Subsequently, platinum decoration is performed via arc plasma deposition (APD). This porous composite structure is then attached to the membrane, and used as the gas diffusion electrode for PEFC membrane electrode assemblies (MEAs). This concept integrates the catalyst, catalyst support, gas diffusion layer, and current collector in a single structure, cutting down on the number of cell components and reducing total device thickness. The carbon-free nature of this integrated gas diffusion electrode is demonstrated to successfully avoid carbon corrosion during start-stop potential cycling over 60,000 potential cycles. However, further improvements in initial electrochemical activity are still required.

Commercialization of fuel cell vehicles (FCVs) has begun in earnest.[1–4] An International Energy Agency (IEA) mobility report in 2017 predicted that by 2040, ca. 9% of global vehicle production would be in the form of FCVs, sharing the market with internal combustion engine vehicles (ICEVs), hybrid electric vehicles (HEVs), plug-in hybrid vehicles (PHEVs), and battery electric vehicles (BEVs).[2] The Hydrogen Council predicts that hydrogen technologies can contribute to a reduction of up to ca. 20% of global CO_2 emissions by 2050.[3] More recently, in 2019, a special report on hydrogen prepared by the IEA was presented at the G20 Energy and Environment Ministerial Meetings held in Japan.[4] This summarized the latest developments and opportunities for hydrogen energy in sectors including transportation, power generation, industry, and local communities. PEFCs are the key technology for realization of the hydrogen economy, carbon-free communities, and zero-emission mobility. As such, further advances in PEFC technologies are highly desirable.

Widespread commercialization of PEFCs will simultaneously require better electrochemical performance, higher power output per system volume, lower production costs, and improved durability. Especially for mobility, competition with ICEVs and BEVs necessitates even better performance, comparable system size, sufficiently high power output (for rapid acceleration), longer driving range, and good lifetime. For better electrochemical performance, advanced electrocatalysts comprising e.g. Pt-alloys[5,6] and core–shell structures[7,8] are promising in order to achieve higher cell voltage under low current density operation, i.e., providing lower activation overvoltage for a given Pt loading. For higher power output, optimization of the porous structure for better mass transport under higher current density operation may be required, i.e., minimizing

the concentration overvoltage and ohmic losses. In order to lower system costs, low-Pt loading and even Pt-free electrocatalysts[9,10] need to be developed.

Compared to BEVs, FCVs are advantageous for heavier duty applications.[4] Besides the passenger vehicles currently being commercialized, heavy duty vehicles such as buses, trucks, trains, and ships are promising applications for PEFCs, where much longer durability and shorter charging time are often required for full utilization of their zero-emission mobility potential. Currently, carbon black is typically used as a catalyst support, but carbon corrosion occurs at the cathode due to start-stop potential cycling (up to 1.5 V vs the reversible hydrogen electrode (RHE)).[11–15] Carbon corrosion results in detachment of Pt catalyst nanoparticles, directly leading to performance degradation.[11] Carbon corrosion can also occur at the anode in e.g. fuel starvation conditions.[12,13] Alternative "carbon-free" catalyst supports are therefore interesting to explore. Electron-conducting oxides are promising, as they are thermochemically stable under strongly acidic conditions and up to high potentials, even at ~80 °C.[16] Examples of such oxides include: TiO_2;[17–24] Ti_4O_7;[25] WO_3;[17,26,27] and SnO_2.[6,17,28–34] Among these candidates, TiO_2 is stable under both cathodic and anodic conditions, but the electronic conductivity is relatively low. Pt nanoparticles supported on TiO_2 are relatively stable against potential cycling, but the catalytic activity is still insufficient, due to poor electronic conductivity.[24] A solution to the problem of conductivity is to use electronically conducting carbon fillers onto which titania and platinum are decorated, decreasing the distance that electrons must travel through the relatively insulating metal oxide phase. However, even when using carbon-based fillers which are physically separated from the TiO_2-supported platinum electrocatalyst, carbon corrosion may still occur to some extent.

Therefore, rather than using carbon black or metal oxides as catalyst supports in PEFCs, we propose here the use of metal

*Electrochemical Society Member.
^{z}E-mail: sasaki@mech.kyushu-u.ac.jp

supports, which could result in improved electronic transport whilst simultaneously completely avoiding carbon corrosion. Many common metals would dissolve in the strongly acidic conditions of a PEFC. However, the thin native oxide layer of titanium is thermochemically stable. This is expected to act as a barrier against dissolution of the underlying metal. As such, titanium is potentially a durable catalyst support for use in PEFCs.

Here, we develop this idea and propose the use of commercially available porous titanium sheets/felts as a basis for the catalyst support, gas diffusion layer, and current collector in PEFC electrodes. In this study, the platinum electrocatalyst is directly deposited onto the porous titanium fiber gas diffusion layer, forming a "gas diffusion electrode." This concept is schematically described in Fig. 1. The use of a porous titanium support is expected to have the following advantages: (i) carbon corrosion will be avoided; (ii) platinum will bind strongly to the native oxide through the strong metal support interaction (SMSI),[35] preventing agglomeration and detachment; (iii) the ohmic resistance will be decreased because of the shorter electronic pathway between the platinum catalyst and the current collector; and (iv) simplified fuel cell manufacture by decreasing the number of cell components. We will systematically study the preparation conditions, investigate the nanostructure of the titanium electrodes, and perform detailed electrochemical characterization, including durability measurements. The advantages and remaining technological issues of using such carbon-free integrated gas diffusion electrodes in MEAs will be discussed and clarified.

Experimental

Chemical etching of titanium sheets.—Commercially available porous titanium sheets (Nikko Techno, Ltd., Japan), as shown in Fig. 2a, made up of interconnecting titanium microfibers were used in this study. The nominal porosity of the sheets was 70%, the thickness was 0.2 mm, and the cross-section of individual titanium fibers was approximately 10 μm by 10 μm. The initial specific surface area of the titanium sheet is only about 1 m^2 g^{-1}.[36] Chemical etching was performed to create nanostructure and increase the area available for catalyst deposition. First, titanium sheets were etched in aqueous NaOH (Kishida Chemical Co., Ltd., Japan) solution at 60 °C for 1 h. The NaOH concentration was varied between 0.1 and 1.0 M. The sample was then washed under ultrasonication in deionized water for 5 min, in 0.01 M HNO$_3$ (Kishida Chemical, Japan) solution for 30 min, and finally again in deionized water at room temperature for 10 min. Heat treatment was then performed at 400 °C in 5% H$_2$-N$_2$ (50 cc min^{-1}) for 30 min with a heating rate of 5 °C min^{-1} up to 400 °C, to improve crystallinity of the nanostructure. Preliminary results reporting the optimization of electrode fabrication conditions were published in Ref. [37].

Electrocatalysts preparation via APD.—Platinum was deposited onto the chemically treated titanium sheets at room temperature, by APD (Advanced RIKO, Inc., Japan). The vacuum pressure was 10^{-3} Pa, the discharge voltage was −100 V, the capacitance was 1080 μF, and the discharge frequency was 3 Hz. The platinum loading was controlled by varying the number of pulses.[36–38] This dry fabrication process was applied in this study, while wet-chemical fabrication procedure is more conventional for Pt catalyst decoration but needs optimization of various preparation conditions.

Characterization of electrodes.—The microstructure of the Pt/Ti electrodes was observed by field emission scanning electron microscopy (FESEM, S-5200, Hitachi High-Technologies, Japan) and scanning transmission electron microscopy (STEM, JEM-ARM200F, JEOL, Japan) in combination with energy dispersive X-ray spectroscopy (STEM-EDS). The acceleration voltages for FESEM and STEM were 30 kV and 200 kV, respectively. Cross sectional samples of electrodes were prepared by focused-ion-beam scanning electron microscopy (FIB-SEM, Versa 3D, FEI). The platinum loading was quantified using inductively coupled plasma
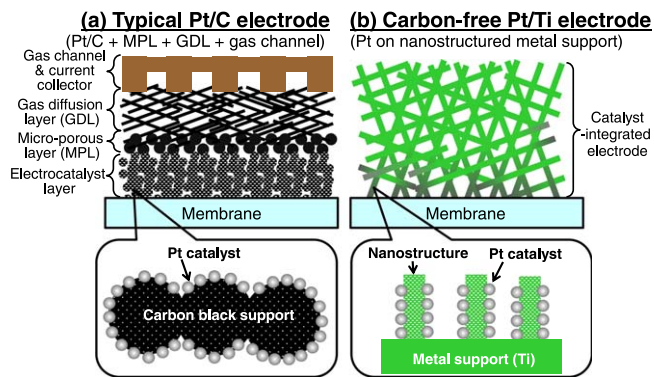

Figure 1. Schematic drawing of (a) a typical PEFC electrode consisting of an electrocatalyst layer, a micro-porous layer (MPL), a gas diffusion layer (GDL), a current collector, and gas channels, and (b) a catalyst-integrated gas diffusion electrode developed in this study.

atomic emission spectroscopy (ICP-AES, ICPE-9000, Shimadzu, Japan), after dissolving the electrodes in aqua regia (HNO$_3$:HCl = 1:3) prepared by mixing 60% HNO$_3$ solution and 35% HCl solution (Kishida Chemical Co., Ltd., Japan).

Electrochemical characterization of electrodes.—The electrochemical activity of the Pt/Ti electrodes was measured using a half-cell setup in acidic electrolyte. Due to the integrated nature of the titanium fiber based electrode system, rotating disk electrode (RDE) voltammetry was not suitable, and therefore static measurements were performed. The working electrode diameter was 3 mm (corresponding to an electrode area of 0.0707 cm^2), and this was connected to a gold wire by spot welding. Electrochemical characterization was performed using an automatic polarization system (HZ-5000, Hokuto Denko Corp., Japan). An Ag/AgCl electrode in saturated KCl was used as the reference electrode, and a Pt wire was used as the counter electrode. The electrolyte solution was 0.1 M HClO$_4$, at 25 °C. Cyclic voltammograms (CV) were evaluated between 0.05 and 1.2 V$_{RHE}$ at 50 mV s^{-1} in N$_2$-saturated HClO$_4$, and all voltages are quoted vs RHE. The electrochemical surface area (ECSA) was determined from the area of the hydrogen desorption peak (Q$_H$ between 0.05 and 0.4 V$_{RHE}$). The oxygen reduction reaction (ORR) activity was inferred from static linear sweep voltammograms (LSVs) at 25 °C in N$_2$-saturated (30 min, 50 cc min^{-1}) and O$_2$-saturated (30 min, 50 cc min^{-1}) HClO$_4$. The potential range was 0.2 to 1.2 V$_{RHE}$, and the scan rate was 10 mV s^{-1}. The current density and the mass activity quoted at 0.9 V$_{RHE}$ were calculated from their average values between 0.85 and 0.95 V$_{RHE}$.

Fabrication of MEAs.—MEAs were prepared with an electrode size of 1.0 cm^2 (1 cm by 1 cm) and a Pt loading of 0.3 mg$_{-Pt}$ cm^{-2} at both the cathode and the anode. Nafion dispersion (Sigma-Aldrich, 5 wt% Nafion in iso-propanol) was deposited onto the nanostructured surface of the titanium sheet by impregnation, before hot-pressing the electrodes at 132 °C and 0.3 kN for 180 s onto one side or both sides of the electrolyte membrane (Nafion 115, 127 μm thickness, Du Pont). The Nafion loading was controlled by diluting the Nafion dispersion with ethanol. For comparison, an MEA using a commercial standard Pt/C electrocatalyst (Pt 46.5%, TEC10E50E, Tanaka Kikinzoku Kogyo Corp., Japan) was measured. A paste was prepared by dispersing Pt/C in a solution of 99.5% ethanol (Kishida Chemical Co., Ltd., Japan), deionized water, and the 5% Nafion dispersion, using an ultrasonic homogenizer. This Pt/C electrocatalyst paste was deposited directly onto the electrolyte membrane using a spray printing system (C-3 J, Nordson). Teflon-coated carbon paper (EC-TP1-060T, Electrochem) was attached as a GDL on one side or both sides of the cell, and the assembly was hot-pressed at 132 °C at 0.3 kN for 180 s.
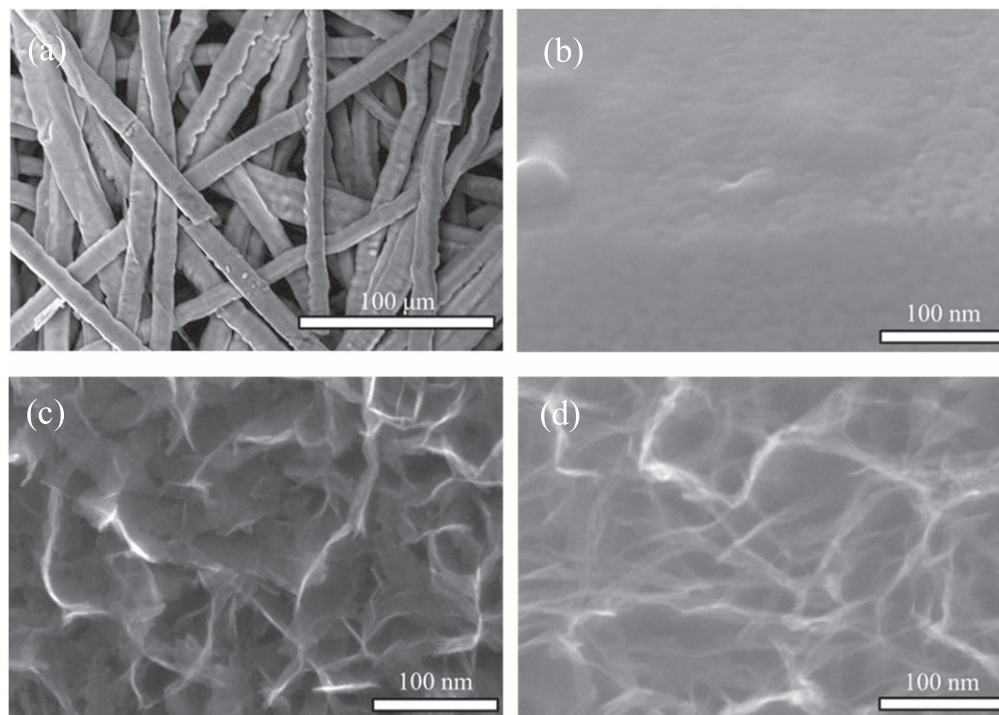
Figure 2. (a) Low-magnification micrograph of the porous titanium sheet used in this study. Individual fibers have a width of ∼10 μm. (b)–(d) FESEM images of the surface of the titanium fibers after NaOH etching at: (b) 0.1 M; (c) 0.5 M; and (d) 1.0 M, followed by heat treatment at 400 °C.

Characterization of MEA performance.—The I-V characteristics of MEAs were evaluated at 80 °C and 100% relative humidity (RH), according to the protocols compiled by New Energy and Industrial Technology Development Organization (NEDO).[39] The cell temperature and gas humidification temperature were both 80 °C. The flow rates of H_2 gas and air were 0.139 cc min^{-1} and 0.332 cc min^{-1}, respectively (corresponding to a stoichiometric ratio of 2:5). A standard cell holder developed in a NEDO project[39] was used for MEA evaluation. Before measurements were taken, the MEAs were pre-treated at 0.6 V for 4 h. I-V characteristics were then measured from open circuit conditions to a cell voltage of 0.3 V, with a sweep rate of 0.5 mA s^{-1} and a step size of 5 mA cm^{-2}. The reproducibility was verified by conducting each measurement three times, and representative data was used for further analysis. The ohmic cell resistance was measured by alternating current (AC) impedance analysis (1255B, Solatron), and the IR losses were separated by subtracting the ohmic contribution from the recorded cell voltage. The IR-free voltage losses were then separated into activation overvoltage and concentration overvoltage, according to the NEDO protocols,[39] as follows. A Tafel plot was created with current density on the logarithmic *x*-axis, and the IR-free cell voltage on the *y*-axis. In the low current density region (below ca. 20 mA cm^{-2}), 3 or 4 values were fitted with a linear regression. The difference between the theoretical electromotive force (1.17 V at 80 °C for a H_2/air cell at ambient pressure) and the voltage of the linear regression line was taken as the activation overvoltage at the current density of interest. The deviation of the IR-free voltage from the voltage in the linear regression line in the Tafel plot was taken as the concentration overvoltage.[39]

MEA durability measurements.—To evaluate the durability of MEAs, accelerated degradation tests were performed. A protocol simulating the start-stop potential cycles of an FCV was used, as recommended by the Fuel Cell Commercialization Conference of Japan (FCCJ) and NEDO.[39–41] According to this protocol, a triangular potential waveform between 1.0 and 1.5 V was used, with 2 s per cycle. At particular points during potential cycling, the ECSA was evaluated from the cyclic voltammograms. In this case, the Pt-based anode was used as a reference electrode, and the potential of the cathode was varied between 0.05 and 0.9 V_{RHE}. The ECSA of the cathode was obtained from analysis of the hydrogen desorption peak area, following the standard NEDO protocols.[39,40] Details on the experimental conditions for these MEA evaluations have been described in our previous studies.[42]

Results and Discussion

***Microstructural characterization of the titanium support.***—Figure 2a shows a low-magnification FESEM micrograph of the commercially available titanium sheet used in this study. The interwoven individual fibers can be observed clearly, with widths of around 10 μm, and lengths extending beyond the scale of the image. Figures 2b to 2d show FESEM images of the titanium fiber surface after NaOH etching at different concentrations, followed by heat treatment at 400 °C. A relatively smooth surface is observed after etching in 0.1 M NaOH (Fig. 2b), indicating that this NaOH solution is not strong enough to modify the titanium surface. After etching in 0.5 M NaOH (Fig. 2c), the appearance of surface features is observed. Bright features of several nanometers in width can be seen, but at this magnification it is unclear if these are nanowires, nanotubes, or vertically aligned nanosheets (see Fig. 7 for higher magnification images). After etching in 1.0 M NaOH (Fig. 2d), a further growth of this nanostructure is observed. This nanostructure is similar to that observed in previous studies where titanium has been etched in NaOH.[43–45]

Figure 3 shows a cross-sectional TEM image of the surface of a titanium fiber after etching in 1.0 M NaOH followed by heat treatment at 400 °C. This image clearly confirms the growth of vertically aligned nanostructure at the titanium fiber surface. The features observed here in the TEM image have widths of around 10 to 20 nm, and heights of around 200 to 400 nm. The introduction of such features is expected to increase the surface area, making these titanium sheets more appropriate as platinum electrocatalyst supports for electrochemical applications.

Figure 4 shows (a) a cross-sectional STEM image of the titanium fiber surface after NaOH etching, with corresponding elemental EDS
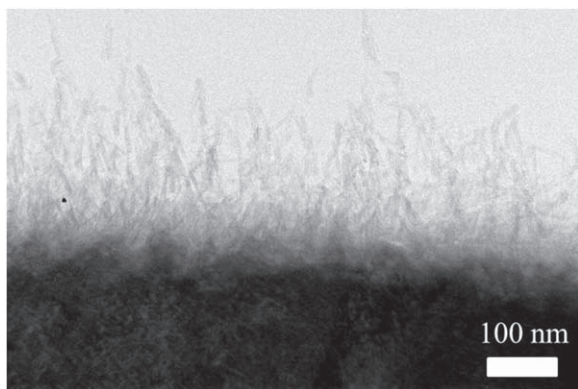
Figure 3. Cross-sectional TEM image of a titanium fiber surface after etching in 1.0 M NaOH, followed by heat treatment at 400 °C.

electrocatalyst layer. As such, the platinum distribution is herein investigated further.

Figure 6 shows (a) a cross-sectional STEM image of the top surface (Region A in Fig. 5) of a platinum-decorated titanium fiber, with corresponding elemental EDS maps of (b) platinum, (c) titanium, and (d) oxygen. In these images, the surface nanostructures appear to be titanium oxide nanotubes. As the EDS signal of titanium and oxygen is relatively weak, higher-contrast EDS images are shown in Figs. 6c and 6d. In Region A, a bright dense layer of platinum coats the nanostructured titanium oxide layer, and is clearly visible in the elemental map (Fig. 6b). Meanwhile, the titanium intensity is low in the surface region of the EDS map (Fig. 6c), due to the high porosity of this nanostructured region. Oxygen is again observed to be present in the surface features, and near the surface of the bulk titanium fiber with a titania thickness of around 50 nm, as shown in Fig. 6d with weak intensity. The higher magnification images shown in Figs. 6e and 6f indicate a uniform coating of

Figure 4. Images of the titanium fiber surface after etching in 1.0 M NaOH followed by heat treatment at 400 °C: (a) STEM image; EDS mapping for (b) titanium (red); and (c) oxygen (blue).

maps of (b) titanium, and (c) oxygen. In general, the EDS signal intensity of oxygen is relatively weak. Otherwise, these images show that the nanostructures formed by the NaOH etching comprise both titanium and oxygen, indicating that the material is likely to be titanium oxide/oxidized titanium. This is in agreement with the literature, where titanium oxide nanotubes have been reported to be formed via the reaction between NaOH and a titanium surface, where titanium nanosheets initially formed tend to curl to form titanium oxide nanotubes.[43–45] Titanium can be observed throughout the bulk and the surface structures. Meanwhile, oxygen is also observed in the surface features, but seems to be mainly concentrated near the surface of the bulk titanium fiber. This suggests that a thin titanium oxide layer is formed at the surface of the titanium fibers.

Platinum decoration by APD.—After etching the surface followed by heat treatment, platinum was subsequently deposited onto the nanostructured titanium sheets by APD. Figure 5 shows a STEM image of a cross section of one titanium fiber etched in 1.0 M NaOH, and decorated with platinum via 2,000 APD pulses. The resulting platinum loading was 0.086 mg_{-Pt} cm^{-2} as measured by ICP-AES. The thin, bright layer on the surface corresponds to the platinum-decorated nanostructured titania. The higher brightness compared to the central part of the titanium fiber is due to the higher atomic mass, and density of platinum, confirming that the APD deposition was successful.

The platinum layer appears to be thickest and brightest at the top surface (Region A), and appears to be thinner on the edges of the titanium fiber (Region B). This inhomogeneity in local platinum distribution is a result of the line-of-sight nature of the APD method. The distribution and connectivity of platinum on the surface of the nanostructured titanium oxide is expected to have an influence on the available catalytic surface area, and electronic transport through the

platinum on each tube-like nanostructure, where platinum almost fully covers the titania nanostructure, suggesting that the electron-conducting pathway though platinum is well established on the surface of these nanofibers.

Higher resolution STEM images of one such nanofiber are shown in Fig. 7. Figure 7a confirms the formation of a titania nanotube, well crystalized after the heat treatment at 400 °C, with an inner diameter of ca. 3 nm and an outer diameter of ca. 15 nm. The lattice fringe indicates that the primary phase is anatase (TiO_2). In addition, Fig. 7b shows that the platinum layer deposited by APD is also well crystallized, with lattice fringes visible in this image. The size of platinum crystallites is a few nm in diameter, similar to the platinum nanoparticles in typical Pt/C electrocatalysts.

Figure 8 shows STEM images from the side of the titanium fiber (Region B in Fig. 5). Here the surface microstructure appears to be sheet-like in nature, and platinum nanoparticles can clearly be distinguished. The relative brightness of platinum (Fig. 8b) on the titania-based nanostructure (Figs. 8c and 8d) is lower compared with Region A (Fig. 6), hinting that the local platinum loading is lower in Region B. In the higher magnification images (Figs. 8e and 8f), individual platinum nanoparticles can be clearly observed. This nanostructure was not observed in Region A, suggesting that the platinum loading at the top surface is too high, forming a more continuous platinum layer, whilst isolated platinum nanoparticles with higher surface area are available in Region B. This is supported by the lower relative intensity in the EDS maps for platinum, as shown in Figs. 8b and 8f.

Half-cell activity.—Figure 9a shows CVs of the titanium fibers etched with different concentrations of NaOH, followed by heat treatment at 400 °C and subsequent platinum decoration by APD (2,000 pulses, 0.086 mg_{-Pt} cm^{-2}). Figure 9b shows the corresponding LSVs (measured under static conditions), and Fig. 9c summarises the ECSA obtained from the CVs, and the apparent
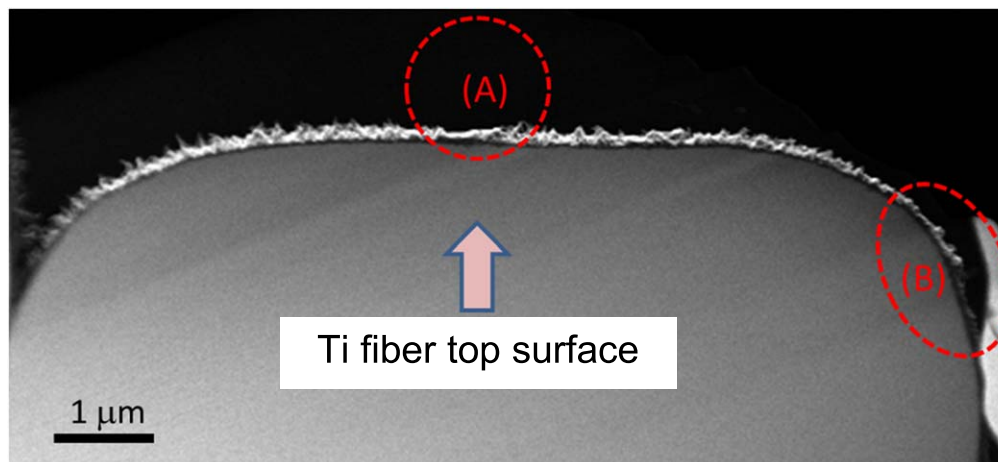
Figure 5. Cross-sectional STEM image of an individual titanium fiber after etching in 1.0 M NaOH followed by heat treatment at 400 °C, and subsequent Pt deposition by APD (2,000 pulses, 0.086 mg$_{-Pt}$ cm^{-2}). Region A corresponds to the top surface, whilst Region B corresponds to the edge of the fiber.

mass activity at 0.9 V$_{RHE}$ (averaged between 0.85 and 0.95 V$_{RHE}$). Due to the difficulty of calculating the mass activity of these unique electrodes using traditional techniques, "apparent mass activity" values measured under static (non-rotating) conditions were calculated from the averaged LSV current (near a potential of 0.9 V$_{RHE}$ in Fig. 9b) divided by the ECSA (Fig. 9c). In contrast to typical rotating disk electrode measurements (RDE), electrode rotation could not be applied for these bulk electrode samples. As such, noise is observed in the LSV curves, so that the curves after smoothing are shown in Fig. 9b. These apparent mass activity values are dependent on e.g. the sweep rate, and as such they are used only for comparing different electrodes measured under the same experimental conditions. There is a slight increase in double layer capacitance in the CVs with increasing NaOH concentration (Fig. 9a), suggesting that etching the titanium sheets results in an increase in surface area due to the formation of nanostructure. The area of the hydrogen desorption peak also increases with increasing NaOH concentration, corresponding to an increase in the ECSA of the supported platinum. This is quantified in Fig. 9c, where a steady increase in ECSA from ~10 to 18 m^2 g^{-1} is observed with increasing NaOH concentration. The increase in ECSA suggests that the dispersion of platinum improves as the surface area of the underlying nanostructured titania increases. Furthermore, the mass activity tends to increase with increasing NaOH concentration, indicating improved utilization of the deposited platinum as the nanostructure of the titanium support is developed. Based on these results, subsequent measurements are made for etching in 1.0 M NaOH.

Figure 10a shows CVs of the titanium fibers etched in 1.0 M NaOH then heat treated, followed by platinum deposition by increasing numbers of APD pulses. By changing the number of APD pulses, the platinum loading could be effectively varied from 0.0043 mg$_{-Pt}$ cm^{-2} (100 pulses) to 0.30 mg$_{-Pt}$ cm^{-2} (7000 pulses). Figure 10b shows the corresponding LSVs, while Fig. 10c summarizes the ECSA obtained from the CVs, and the mass activity (at 0.9 V$_{RHE}$) from the LSVs.

The double layer capacitance increases slightly with the number of APD pulses (Fig. 10a) indicating that platinum decoration slightly increases the surface area or the capacitance of the electrode. The area of the hydrogen desorption peak significantly increases as the number of pulses increases, corresponding to an overall increase in total available area for hydrogen adsorption. However, it should be noted that in this case, the platinum loading also increases, so this does not correspond to an increase in the ECSA. Indeed, the ECSA actually decreases from ~40 to 8 m^2 g^{-1} as the number of pulses increases as shown in Fig. 10c. This is as expected, since increasing the connectivity between platinum nanoparticles as the loading increases will decrease the available platinum surface for hydrogen

adsorption. Meanwhile, the current density (at 0.9 V$_{RHE}$) increases with increasing number of pulses (Fig. 10b), as expected due to the increased platinum loading. In contrast, Fig. 10c shows that the mass activity starts very low, rising rapidly as the number of pulses is increased to 1000, after then gradually decreasing between 1000 and 7000 pulses. The initial increase in mass activity may be attributed to increasing catalytic activity of Pt nanoparticles. Meanwhile, the subsequent decrease in mass activity is attributed to the increasing agglomeration (as reflected by decreasing ECSA), decreasing the availability of surface platinum atoms for the ORR to take place at.

Single-cell MEA performance.—MEAs were prepared using titanium sheets etched in 1.0 M NaOH, followed by heat treatment at 400 °C, and subsequent platinum decoration by APD (7,000 pulses). Table I summarizes the type of electrode and the ionomer content for each of six MEAs tested. Ionomer loading is also shown in Table I. MEA#1 is a reference cell and uses the commercial standard Pt/C electrocatalyst at both electrodes. MEA#2 and MEA#3 used a combination of Pt/C and Pt/Ti electrodes. MEA#4, MEA#5, and MEA#6 all used Pt/Ti for both electrodes, with different ionomer contents.

Figure 11 summarizes: (a) the I-V characteristics; (b) the activation overvoltage; (c) the concentration overvoltage; and (d) the ohmic overvoltage (i.e. IR losses) for all of these MEAs. The graphs in Fig. 11 show the actual data points connected by lines, and not fitted lines. The typical standard deviation was e.g. 20 mV for an average cell voltage of 0.418 V at 100 mA cm^{-2}, for MEA#4 in Fig. 11a. The current densities achieved here are relatively low compared to conventional MEAs, in all cases. This is attributed in part to the relatively thick Nafion membranes (127 μm thickness) resulting in higher ohmic resistance. These were used to ensure that no short circuiting occurred between titanium fibers from both electrodes.

Comparing MEA#1 and #2, there is only a slight decrease in performance for the cell using a Pt/Ti anode compared with the Pt/C reference, but the losses are greater at higher current density. The activation overvoltage is similar in both cases. However, the concentration overvoltage deviates significantly at high current density. This suggests that mass transport limitation is the main culprit for the performance loss. Mass transport is strongly affected by microstructure, and therefore the concentration overvoltage is attributed to the lower surface area and porosity of the Pt/Ti anodes and/or cathodes compared with conventional carbon black based electrodes. The higher concentration overvoltage could arise due to relatively thick Nafion ionomer layer due to the much lower macroscopic surface area of the catalyst support in this case. In addition, there is a slight increase in ohmic resistance. The
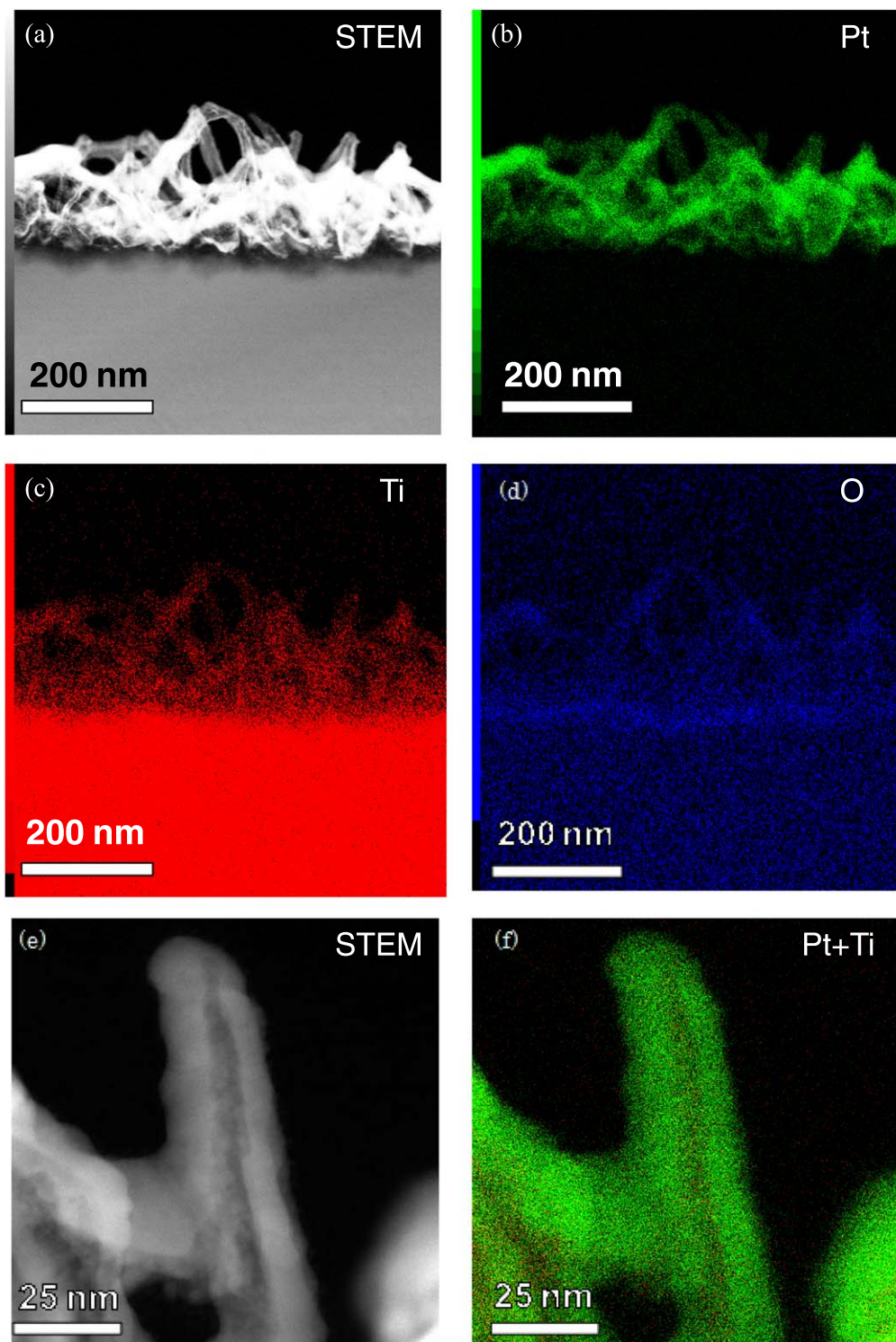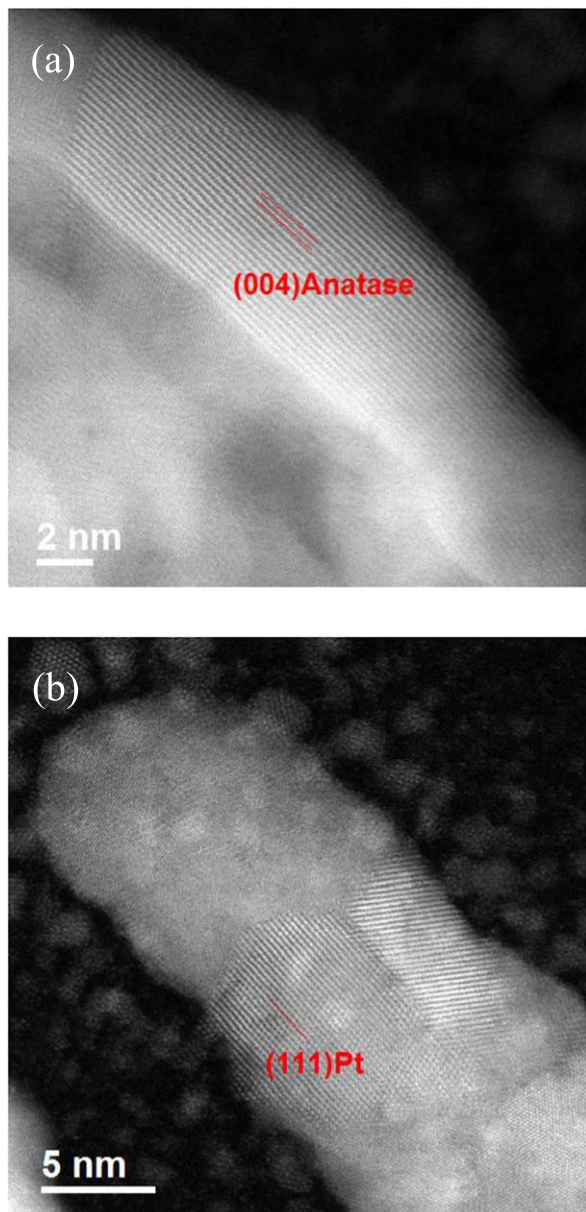
Figure 6. STEM images of the titanium fiber surface after etching in 1.0 M NaOH, followed by heat treatment at 400 °C, and subsequent platinum deposition by APD (2,000 pulses, 0.086 mg$_{-Pt}$ cm^{-2}). These images were recorded in Region A (i.e. at the top surface of the fiber): (a) STEM image; EDS maps for (b) platinum (green), (c) titanium (red, higher-contrast image), and (d) oxygen (blue, higher-contrast image); (e) a higher-magnification STEM image, and (f) the corresponding EDS map for platinum (green) and titanium (red).

membrane is the same in both cases, and the electronic resistivity of titanium (ca. 4×10^{-7} Ω m) is lower than that of bulk graphite (ca. 2×10^{-5} Ω m) at room temperature.[46] The small increase in ohmic resistance could be attributed to increased resistance within the Pt/Ti electrode due to e.g. the layer of oxidized titanium with higher electronic resistance, as observed in EDS mapping (Figs. 4c and 6d). Interfacial resistances could also increase the ohmic resistance.

Using Pt/C at the anode and Pt/Ti at the cathode (MEA#3) results in a more significant performance drop, despite the structure effectively being the same as in MEA#2. This immediately highlights that the Pt/Ti system needs more optimization for use at the cathode compared with the anode. The activation overvoltage increases in MEA#3 compared to the reference MEA#1. One reason could be a geometric effect, where the surface area of the catalyst

Figure 7. Higher-resolution STEM images of a titanium fiber after etching in 1.0 M NaOH, followed by heat treatment at 400 °C, and subsequent platinum deposition by APD (2,000 pulses, 0.086 mg$_{-Pt}$ cm^{-2}). These images were recorded in Region A (i.e. at the top surface of the titanium fiber).

support was small, leading to lower ECSA. Other reasons could be substrate-related effects, i.e. that electron transfer in the local region around the cathode electrocatalyst may be suppressed due to the presence of insulating titanium oxide; or that the catalytic activity at the cathode is suppressed due to the strong metal-support interaction (SMSI).[35] The concentration overvoltage increases significantly compared to the cases of MEA#1 and MEA#2, suggesting that e. g. the hydrophilicity of titanium oxide may cause local water flooding at the cathodes. Meanwhile, the ohmic overvoltage in MEA#3 is exactly the same as for MEA#2. This is as expected, since the structure is essentially the same only with the nominated electrodes reversed.

Switching to the use of Pt/Ti at both electrodes (whilst keeping the Nafion content constant for the cathode) results in another slight drop in I-V performance for MEA#4. In this case there is a further increase in activation overvoltage, suggesting that the Nafion content may be too high in this iteration and that the insulting titanium oxide

still interferes with the catalytic reactions. There is only a slight increase in concentration overvoltage for MEA#4 compared with MEA#3, which is mainly attributed to the anodes, which have different ionomer contents as listed in Table I. The ohmic over-voltage (IR loss) for MEA#4 is similar to the cases of MEA#1 and MEA#2, showing that the contribution of the resistance of titanium oxide is relatively small within the total cell resistance.

Decreasing the Nafion content from 20 to 10 μl cm^{-2} results in a slight improvement in the I-V characteristics of MEA#5 compared to MEA#4. This is accompanied by a slight decrease in activation overvoltage, suggesting improved accessibility to the platinum catalyst as the Nafion coverage decreases. A significant decrease in concentration overvoltage is observed, similarly suggesting that gas accessibility to active sites is improved by decreasing the Nafion content. A slight increase in ohmic resistance indicates that the proton pathway in the electrocatalyst layer is affected by the decrease in ionomer coverage. Finally, decreasing the Nafion content from 10 to 5 μl cm^{-2} results in the greatest loss of performance (MEA#6). A major increase in activation overvoltage is observed, suggesting a lack of available protons at the Pt catalysts due to insufficient Nafion content in the electrocatalyst layer, on top of the limited electron transfer due to the insulating titanium oxide layer. Such bottlenecks in local mass transport may also be attributed to the increase in concentration overvoltage. In addition, the ohmic resistance increases, partly because of the poor proton conducting pathway in the electrocatalyst layer. While the titanium fibers provide an electron-conducting pathway and porous gas transport channels, proton transport occurs via the impregnated Nafion ionomer. Insufficient Nafion coverage may result in low platinum utilization due to limited supply of protons. However, excess Nafion ionomer may also result in low Pt utilization due to insufficient oxygen supply at the cathode (and insufficient hydrogen supply at the anode). As such, the ionomer loading should be carefully considered and optimized.

The above results indicate that (i) a Nafion loading of 10 μl cm^{-2} was optimal for the Pt/Ti MEAs but further optimization of the ionomer distribution is desirable; (ii) high activation overvoltage (especially at the cathode) is a major issue for further improvement; (iii) the microstructure of the titanium fiber surface should be further optimized to minimize the concentration overvoltage; and (iv) the electronic conductivity of titanium oxide should be improved. However, overall these results are an important proof-of-concept for this unique carbon-free, integrated electrode design for MEAs. In future studies, we aim to improve and control some of the properties of the Pt/Ti structure by e.g. further optimizing the etching procedures and conditions; doping the titanium oxide with donor atoms to improve the electronic conductivity; chemically reducing the titanium oxide to e.g. Ti$_4$O$_7$ to improve the electronic conductivity; forming titanium oxy-nitrides also with higher electronic conductivity; and/or reducing the thickness of porous metal sheets for improving volumetric power density.

The surface area to bulk ratio was improved by inducing nanostructure at the titanium fiber surface. However, as shown in Fig. 5, the induced nanostructure is limited to a thin film at the surface. In addition, the line-of-sight nature of APD means that platinum is concentrated near the top surface of the porous titanium sheets. As such, further improvements in activity can be expected if the surface area to bulk ratio is increased (e.g. by using titanium fibers with smaller diameter or significantly increasing the thickness of the nanostructured surface). These concepts are now under investigation.

Start-stop cycling durability.—Improving the durability is one of the most important issues facing the commercialization of PEFCs. Due to the absence of carbon in this novel titanium-based MEA, it is expected that carbon corrosion can be completely avoided. As such, we investigated the durability of our integrated electrode system during 60,000 start-stop potential cycles between 1.0 and 1.5 V$_{RHE}$, corresponding to the typical lifetime of an FCV.[40,41] Figure 12a
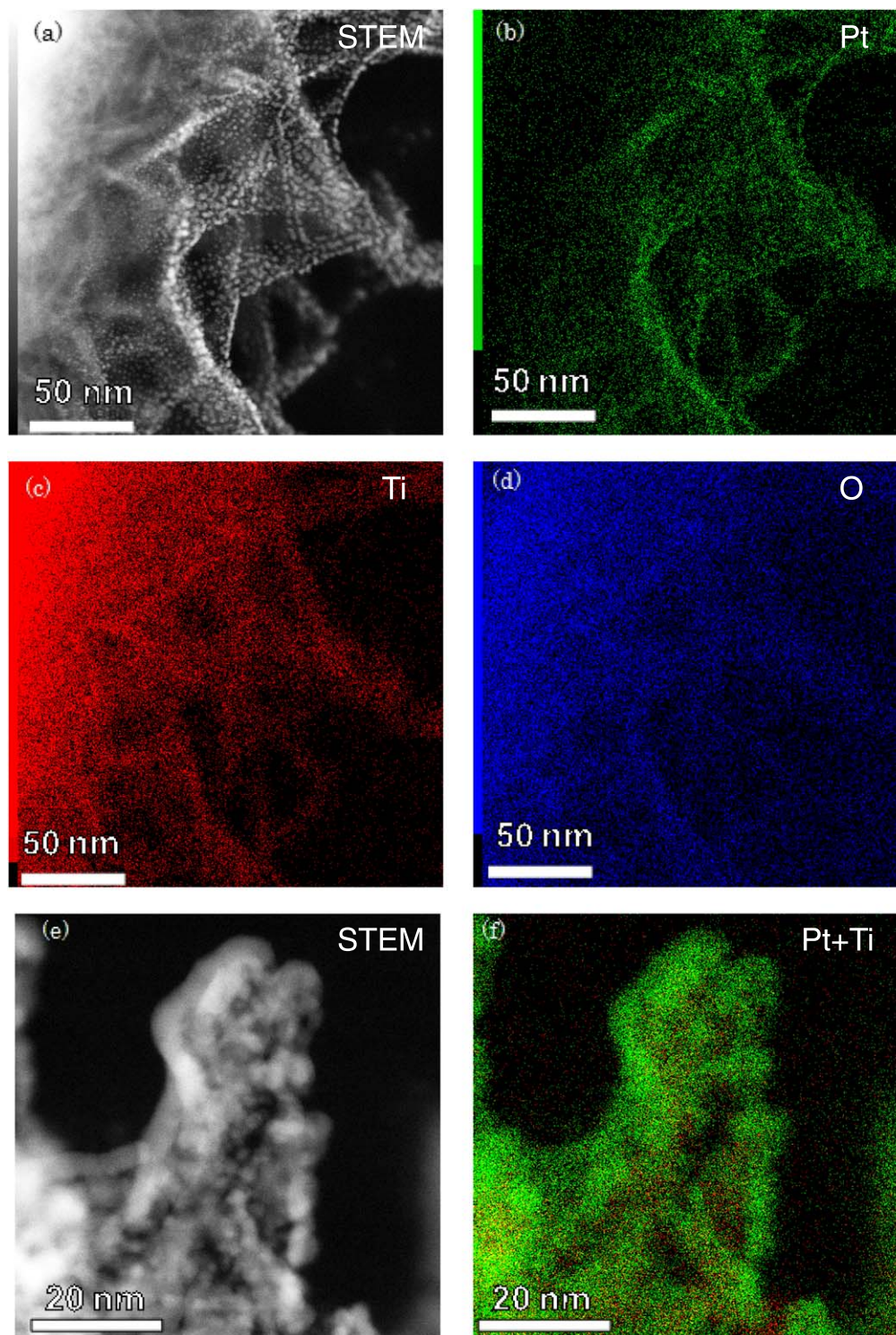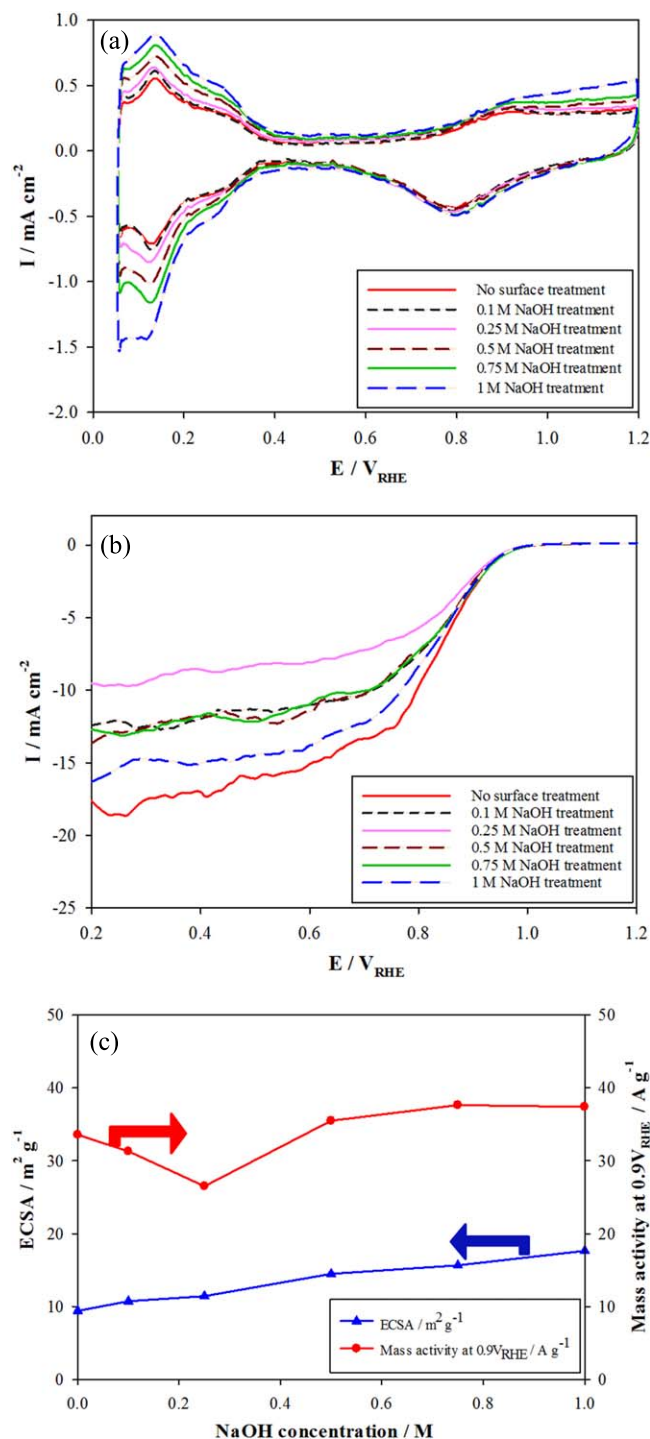
Figure 8. STEM images of the titanium fiber surface after etching in 1.0 M NaOH, followed by heat treatment at 400 °C, and subsequent platinum deposition by APD (2,000 pulses, 0.086 mg$_{-Pt}$ cm^{-2}). These images were recorded in Region B (i.e. on the sides of the titanium fiber): (a) STEM image; EDS maps for (b) platinum (green), (c) titanium (red, higher-contrast image), (d) oxygen (blue, higher-contrast image); (e) higher-magnification STEM image, and (f) the corresponding EDS map for platinum (green) and titanium (red).

shows the evolution of the ECSA in a conventional Pt/C based fuel cell (MEA#1), whilst Fig. 12b shows the I-V characteristics. The initial ECSA in this cell was 57 m^2 g^{-1}, but this value quickly decreased to 38 m^2 g^{-1} after just 2,000 cycles. The ECSA then gradually decreased to 29 m^2 g^{-1} after 60,000 cycles. This decrease in ECSA is accompanied by a severe performance loss in the I-V

plots, as shown in Fig. 12b. For example, the cell voltage at 0.2 A cm^{-2} decreased from 0.6 to 0.3 V after just 2,000 cycles.

Meanwhile, for the carbon-free Pt/Ti system (Figs. 12c and 12d), the initial ECSA was significantly lower, at around 12 m^2 g^{-1}. However, in contrast to the Pt/C system, the ECSA actually increased over the first 2,000 potential cycles in the titanium-based system. We have previously discussed a similar initial increases in
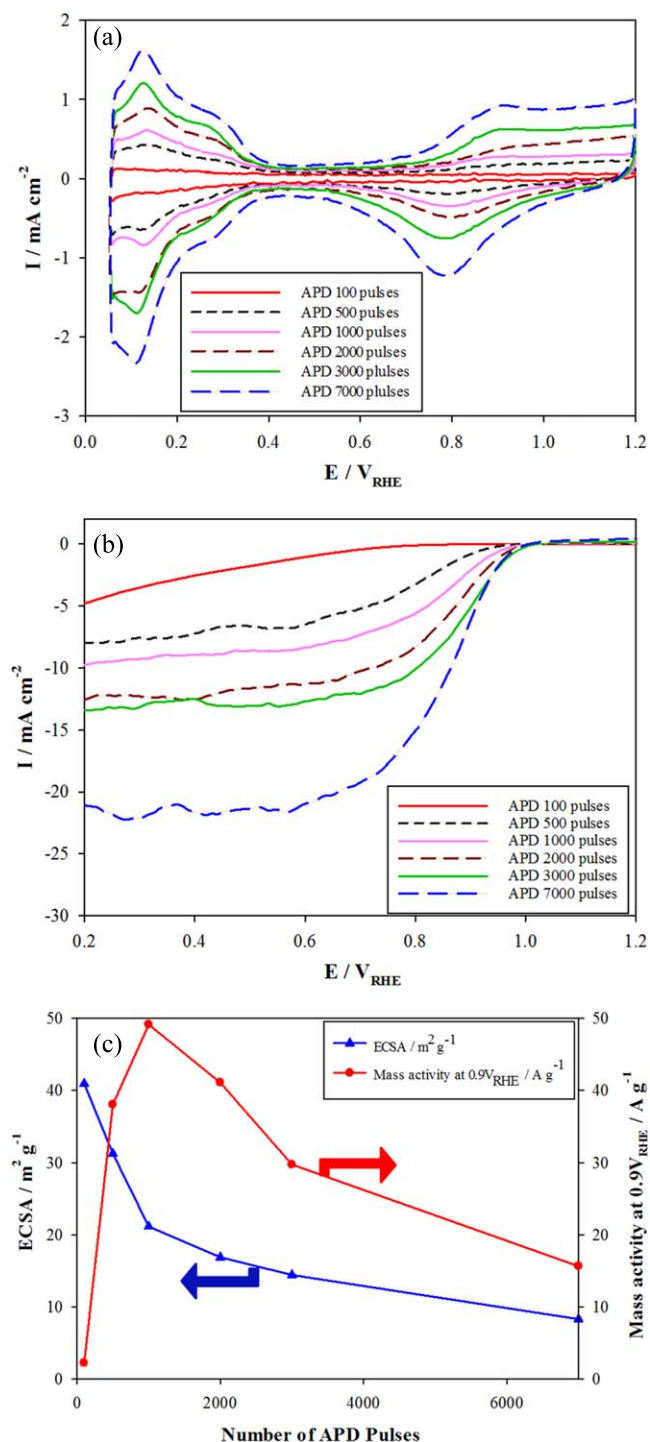
Figure 9. Electrochemical properties of the titanium sheet electrodes etched in NaOH at various concentrations, followed by heat treatment at 400 °C and subsequent platinum deposition by APD (2000 pulses, 0.086 $mg_{\text{-Pt}}$ cm^{-2}): (a) cyclic voltammetry; (b) linear sweep voltammetry; and (c) summary of the ECSA and the mass activity at 0.9 V_{RHE}.
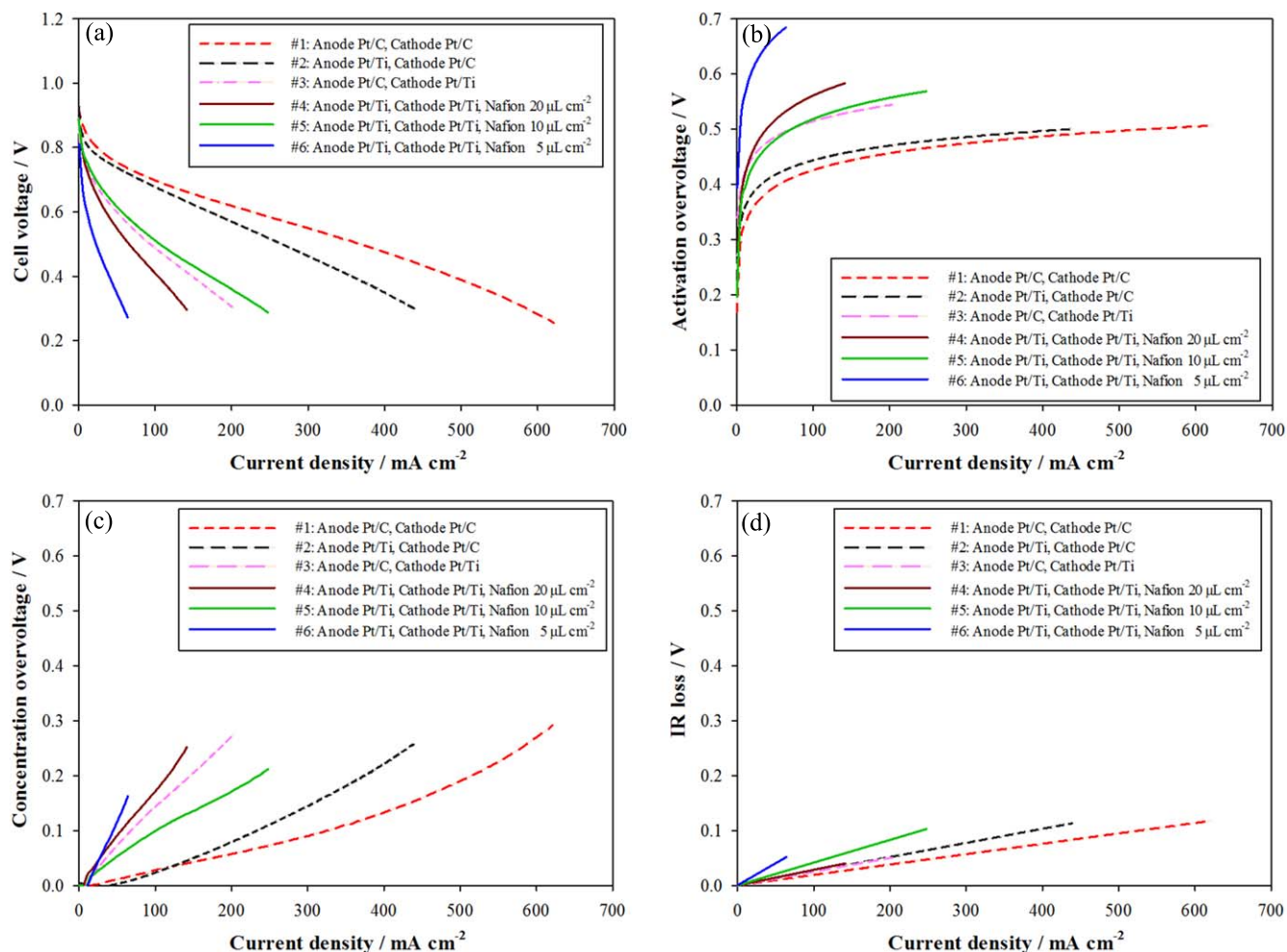
Figure 10. Electrochemical properties of the titanium sheet electrodes etched in 1.0 M NaOH, followed by heat treatment at 400 °C and subsequent platinum deposition by different numbers of APD pulses (between 100 and 7000): (a) cyclic voltammetry; (b) linear sweep voltammetry; and (c) summary of the ECSA and the mass activity at 0.9 V_{RHE}.

ECSA for metal oxide-supported electrocatalysts.[47,48] The ECSA then does not change significantly over the whole 60,000 potential cycles. At the same time, as shown in Fig. 12d, there is a small initial improvement in the I-V characteristics, followed by relatively stable operation over the whole durability test.

As such, it is clear that, whilst the initial performance of Pt/C based MEAs is higher than that of Pt/Ti based MEAs, carbon corrosion quickly leads to performance degradation. The carbon-free

nature of the Pt/Ti system results in stable operation because carbon corrosion does not occur. The negligible performance degradation of the titanium system indicates the potential of such carbon-free electrodes in fundamentally solving the problem of carbon corrosion. However, whilst this is an important proof-of-concept, the initial ECSA and I-V characteristics are still insufficient. As such, (i) improving the nano- and microstructure to increase the surface area of these novel titanium-based electrodes, and (ii) controlling

Table I. Summary of the fabrication conditions for 6 different MEAs tested.

MEA no.	Electrode + GDL		Ionomer, 5% solution ($\mu l\ cm^{-2}$)		Ionomer loading (wt%)	
	Anode	Cathode	Anode	Cathode	Anode	Cathode
#1	Pt/C + carbon paper	Pt/C + carbon paper	5.8	5.8	28	28
#2	Pt/Ti	Pt/C + carbon paper	20	5.8	3.1	28
#3	Pt/C + carbon paper	Pt/Ti	5.8	20	28	3.1
#4	Pt/Ti	Pt/Ti	20	20	3.1	3.1
#5	Pt/Ti	Pt/Ti	10	10	1.6	1.6
#6	Pt/Ti	Pt/Ti	5.0	5.0	0.8	0.8

Figure 11. Electrochemical performance of novel MEAs fabricated using combinations of the platinum-decorated surface-etched titanium sheet electrodes (Pt/Ti): (a) I-V characteristics; (b) activation overvoltage; (c) concentration overvoltage; and (d) ohmic overvoltage (IR loss). In all cases, the titanium sheets were etched in 1.0 M NaOH followed by heat treatment at 400 °C and subsequent platinum deposition using APD (7000 pulses). The Pt loading was 0.3 $mg_{-Pt}\ cm^{-2}$ for both electrodes, and a Nafion 115 membrane (127 μm thickness) was used in all cases. Tests were performed at 80 °C, under fully humidified conditions. The ohmic resistance of MEAs shown in (d) ranges from 0.166 (MEA#1) to 0.275 Ω (MEA#6) for a 1 cm^2 electrode.

hydrophilicity/hydrophobicity to prevent water flooding, will be the main focuses of future research. Development of wet-chemical fabrication procedures (as opposed to APD) may also be desirable for future large-scale mass production of such catalyst-integrated gas diffusion electrodes and their cell/stacks. Evaluation of these electrodes using alternative protocols (e.g. the Department of Energy recommendations for catalyst support tests using a potential hold at 1.2 V) will be helpful for comparison with data reported in the literature.[49] An economic comparison between titanium-fiber based GDEs and conventional carbon-fiber based GDLs is also an important issue for future analysis, and will depend on the capital cost of titanium fibers vs carbon fibers, and on MEA fabrication costs.

Conclusions

Carbon-free catalyst-integrated nanostructured electrodes with porous titanium metal supports were developed for PEFCs. Commercially available porous titanium sheets were etched in NaOH and heat-treated at 400 °C. This resulted in the formation of titanium oxide nanostructures on the surface of the individual titanium fibers. Platinum was then deposited onto the surface of the fibers via APD. This structure was then used as a carbon-free
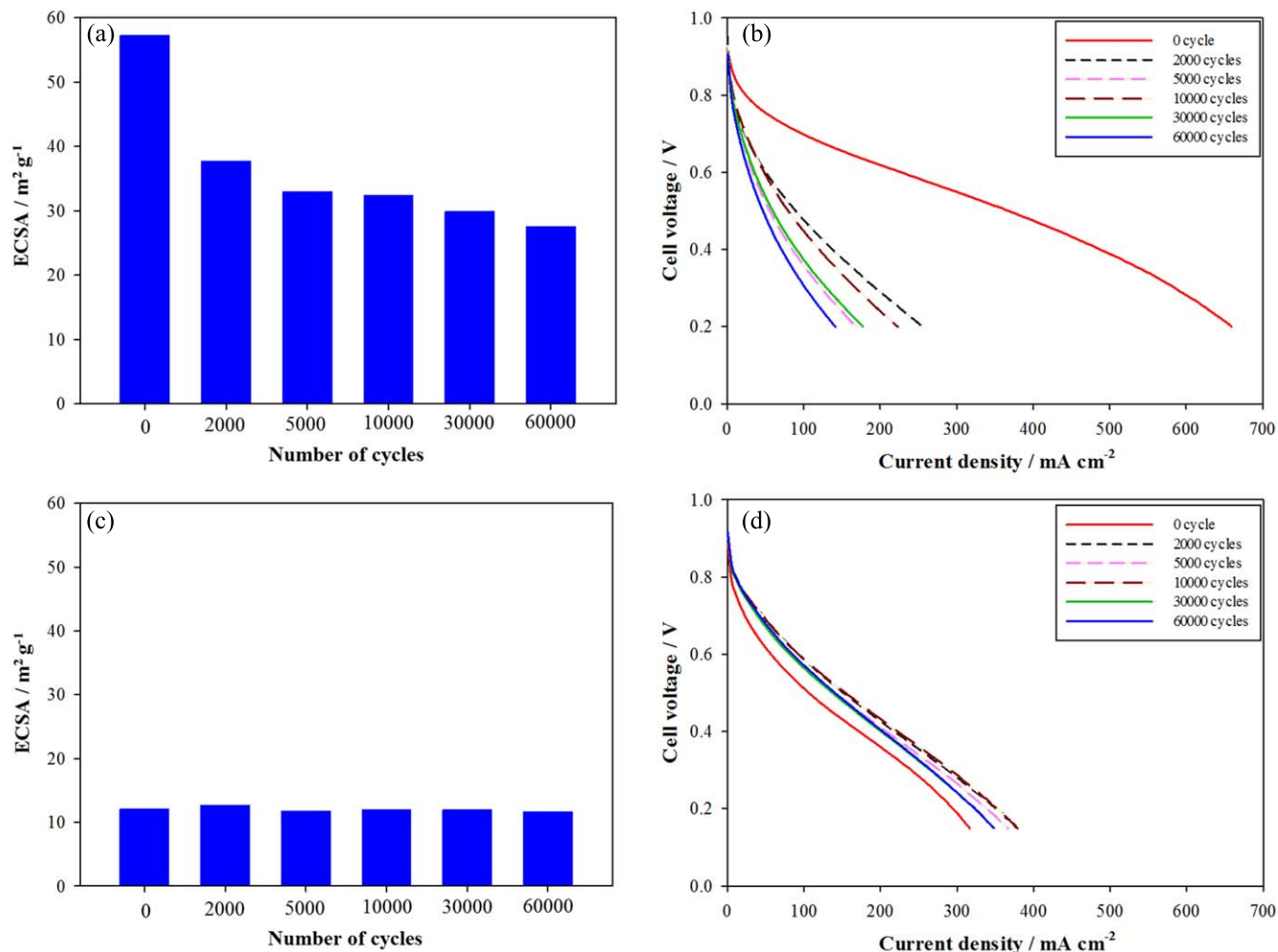
Figure 12. (a) ESCA and (b) I-V characteristics of the Pt/C fuel cell (MEA#1) over 60,000 start-stop durability potential cycles. (c) ESCA and (b) I-V characteristics of the Pt/Ti fuel cell (MEA#5) over 60,000 start-stop potential cycles.

integrated gas diffusion electrode for a fuel cell MEA with a Nafion membrane. The platinum-decorated nanostructured titanium sheets acted simultaneously as the catalyst, catalyst support, gas diffusion layer, and current collector, whilst avoiding the problem of carbon corrosion. Whilst the initial activity of the titanium MEA system was lower than that of a conventional Pt/C system, the system showed remarkable durability during start-stop potential cycling. As such, this technology may be promising for e.g. heavy duty FCV applications. However, improvement of the initial activity by optimizing the system to minimize voltage losses is one of the important next steps.

ORCID

A. Hayashi https://orcid.org/0000-0003-1753-2241
K. Sasaki https://orcid.org/0000-0002-3174-9087

References

1. K. Sasaki, H.-W. Li, A. Hayashi, J. Yamabe, T. Ogura, and S. M. Lyth, *Hydrogen Energy Engineering: A Japanese Perspective* (Springer, Japan) (2016).

2. International Energy Agency, *Energy Technology Perspectives 2017 - Catalysing Energy Technology Transformations*, June 2017, https://webstore.iea.org/energy-technology-perspectives-2017 (accessed 2019. 10. 25).

3. Hydrogen Council, *Hydrogen, Scaling Up*, November 2017, https://hydrogen-council.com/wp-content/uploads/2017/11/Hydrogen-Scaling-up_Hydrogen-Council_2017.compressed.pdf (accessed 2019. 10. 25).

4. International Energy Agency, The Future of Hydrogen - Seizing today's opportunities, Report prepared by the IEA for the G20, Japan, June 2019, https://www.iea.org/hydrogen2019/ (accessed 2019. 10. 25).

5. U. S. Paulus, A. Wokaun, and G. G. Scherer, *J. Phys. Chem. B*, **106**, 4181 (2002).

6. S. Matsumoto, M. Nagamine, Z. Noda, J. Matsuda, S. M. Lyth, A. Hayashi, and K. Sasaki, *J. Electrochem. Soc.*, **165**, F1165 (2018).

7. J. Zhang, F. H. B. Lima, M. H. Shao, K. Sasaki, J. X. Wang, J. Hanson, and R. R. Adzic, *J. Phys. Chem. B Lett.*, **109**, 22701 (2005).

8. M. Inaba and H. Daimon, *ECS Trans.*, **50**, 65 (2013).

9. B. Wang, *J. Power Sources*, **152**, 1 (2005).

10. J. Kim, A. Ishihara, S. Mitsushima, N. Kamiya, and K. Ota, *Electrochemica Acta*, **52**, 2492 (2007).

11. L. M. Roen, C. H. Paik, and T. D. Jarvi, *Electrochem. Solid-State Lett.*, **7**, A19 (2004).

12. C. A. Reiser, L. Bregoli, T. W. Patterson, J. S. Yi, J. D. Yang, M. L. Perry, and T. D. Jarvi, *Electrochem. Solid-State Lett.*, **8**, A273 (2005).

13. J. P. Meyers and R. M. Darling, *J. Electrochem. Soc.*, **153**, A1432 (2006).

14. T. Kinumoto, K. Takai, Y. Iriyama, T. Abe, M. Inaba, and Z. Ogumi, *J. Electrochem. Soc.*, **153**, A58 (2006).

15. S. Maass, F. Finsterwalder, G. Frank, R. Hartmann, and C. Merten, *J. Power Sources*, **176**, 444 (2008).

16. K. Sasaki, F. Takasaki, Z. Noda, S. Hayashi, Y. Shiratori, and K. Ito, *ECS Tran.*, **33**, 473 (2010).

17. Y. Takabatake, Z. Noda, S. M. Lyth, A. Hayashi, and K. Sasaki, *Intl. J. Hydrogen Energy*, **39**, 5074 (2014).

18. T. Kuroki, K. Sasaki, H. Kusaba, and Y. Teraoka, (2004), *Extended Abstract#1527, 206th Meeting of Electrochem. Soc.*, Hawaii https://www.electrochem.org/dl/ma/206/pdfs/1527.pdf.

19. K. W. Park and K. S. Seol, *Electrochem. Comm.*, **9**, 2256 (2007).
20. B. L. Garcia, R. Fuentes, and J. W. Weidner, *Electrochem. Solid-State Lett.*, **10**, B108 (2007).
21. N. Rajalakshmi, N. Lakshmi, and K. S. Dhathathreyan, *Intl. J. Hydrogen Energy*, **33**, 7521 (2008).
22. S. L. Gojkovic, B. M. Babic, V. R. Radmilovic, and N. V. Krstajic, *J. Electroanal. Chem.*, **639**, 161 (2010).
23. S. Y. Huang, P. Ganesan, and B. N. Popov, *Appl. Catal. B. Environ.*, **102**, 71 (2011).
24. M. Iwami, D. Horiguchi, Z. Noda, A. Hayashi, and K. Sasaki, *ECS Trans.*, **69**, 603 (2015).
25. T. Ioroi, Z. Siroma, N. Fujiwara, S. Yamazaki, and K. Yasuda, *Electrochem. Comm.*, **7**, 183 (2005).
26. H. Chhina, S. Campbell, and O. Kesler, *J. Electrochem. Soc.*, **154**, B533 (2007).
27. X. Cui, H. Zhang, X. Dong, H. Chen, L. Zhang, L. Guo, and J. Shi, *J. Mater. Chem.*, **18**, 3575 (2008).
28. W. Quang Han and A. Zettl, *Nano Lett.*, **3**, 681 (2003).
29. W. S. Baker, J. J. Pietron, M. E. Teliska, P. J. Bouwman, D. E. Ramaker, and K. E. Swider-Lyons, *J. Electrochem. Soc.*, **153**, A1702 (2006).
30. M. Nakada, A. Ishihara, S. Mitsushima, N. Kamiya, and K. Ota, *Electrochem. Solid-State Lett.*, **10**, F1 (2007).
31. K. Kakinuma, Y. Senoo, K. Taniguchi, M. Watanabe, and M. Uchida, *J. Electrochem. Soc.*, **165**, J3083 (2018), *228th ECS Meeting Abstract*, 1558.
32. X. Li, J. Wei, Y. Chai, and S. Zhang, *J. Colloid and Interface Sci.*, **450**, 74 (2015).
33. P. K. Mohana, C. Glokler, A. O. Arenas, and L. Jonssen, *Intl. J. Hydrogen Energy*, **42**, 27950 (2017).
34. Y. Nakazato, D. Kawachino, Z. Noda, J. Matsuda, S. M. Lyth, A. Hayashi, and K. Sasaki, *J. Electrochem. Soc.*, **165**, F1154 (2018).
35. T. Daio, A. Staykov, L. Guo, M. Tanaka, S. M. Lyth, and K. Sasaki, *Sci. Rep.*, **5**, 13126 (2015).
36. M. Yasutake, D. Kawachino, Z. Noda, J. Matsuda, K. Ito, A. Hayashi, and K. Sasaki, *ECS Trans.*, **92**, 833 (2019).
37. D. Kawachino, Z. Noda, J. Matsuda, A. Hayashi, and K. Sasaki, *ECS Trans.*, **80**, 781 (2017).
38. T. Ito, M. Kunimatsu, S. Kaneko, Y. Hirabayashi, M. Soga, Y. Agawa, and K. Suzuki, *Talanta*, **99**, 865 (2012).
39. Daido University, Ritsumeikan University, Tokyo Institute of Technology, and Japan Automobile Research Institute, *Cell Evaluation and Analysis Protocol Guideline (Electrocatalyst, Support, Membrane and MEA)* (New Energy and Industrial Technology Development Organization (NEDO), Japan) (2014).
40. New Energy and Industrial Technology Development Organization (NEDO), https://nedo.go.jp/content/100537904.pdf (accessed 2019. 10. 17).
41. A. Ohma, K. Shinohara, A. Iiyama, T. Yoshida, and A. Daimaru, *ECS Trans.*, **41**, 775 (2011).
42. M. Okumura, Z. Noda, J. Matsuda, Y. Tachikawa, M. Nishihara, S. M. Lyth, A. Hayashi, and K. Sasaki, *J. Electrochem. Soc.*, **164**, F928 (2017).
43. Y. Q. Wang, G. Q. Hu, X. F. Duan, H. L. Sun, and Q. K. Xue, *Chem. Phys. Lett.*, **365**, 427 (2002).
44. Y. F. Chen, C. Y. Lee, M. Y. Yeng, and H. T. Chiu, *Mater. Chem. Phys.*, **80**, 39 (2003).
45. Q. Chen, G. H. Du, S. Zhang, and L. M. Peng, *Acta Cryst.*, **B58**, 587 (2002).
46. D. R. Lide, *CRC Handbook of Chemistry and Physics* (CRC Press, Taylor & Francis Group, Howick Place, London) 89th ed. (2008).
47. F. Takasaki, S. Matsuie, Y. Takabatake, Z. Noda, A. Hayashi, Y. Shiratori, K. Ito, and K. Sasaki, *J. Electrochem. Soc.*, **158**, B1270 (2011).
48. A. Masao, S. Noda, F. Takasaki, K. Ito, and K. Sasaki, *Electrochem. Solid-State Lett.*, **12**, B119 (2009).
49. Department of Energy, *DOE Cell Component Accelerated Stress Test Protocols for PEM Fuel Cells (Electrocatalysts, Supports, Membranes, and Membrane Electrode Assemblies)*, March 2007, https://www1.eere.energy.gov/hydrogenandfuelcells/fuelcells/pdfs/component_durability_profile.pdf (accessed 2020. 6. 1).